Coble creep in heterogeneous materials: The role of grain boundary engineering

Ying Chen and Christopher A. Schuh*
Department of Materials Science and Engineering, Massachusetts Institute of Technology, 77 Massachusetts Avenue, Cambridge, Massachusetts 02139, USA
(Received 14 May 2007; published 14 August 2007)

Grain boundary engineering methods improve materials properties by modifying the composition and connectivity of grain boundary networks. A quantitative understanding of grain boundary network characteristics and their impact on materials properties is therefore desirable for both scientific and practical purposes. In this paper, we focus on the case of Coble creep, a viscous deformation mechanism prevailing at intermediate to high temperatures. Using computer simulations, we characterize the creep viscosity as a function of the fraction of slow-diffusing "special" grain boundaries in a two-dimensional honeycomb grain boundary network. This basically defines a new class of percolation problem where mass diffusion and force equilibrium are coupled in a complex way. The percolation threshold and scaling exponents are extracted from the simulation data and analyzed in the context of correlations and energy balance on the network. We also explore stress concentrations induced by the grain boundary character distribution, the effect of crystallographic constraints, and an empirical effective-medium equation that may be used with classical creep constitutive laws in order to predict the viscosity of a heterogeneous material.

DOI: 10.1103/PhysRevB.76.064111 PACS number(s): 62.20.Hg, 64.60.Ak, 61.72.Mm, 81.40.−z

I. INTRODUCTION

There is generally a wide distribution of grain boundary character in polycrystalline materials, including variations in misorientation and plane inclination.[1] The species as well as the spatial distribution of diverse grain boundary types control interface-related properties such as intergranular degradation[2,3] and creep.[4–7] In some cases, the grain boundary character distribution (GBCD) of metallic materials can be modified by proper processing treatments.[8–10] Such "grain boundary engineering" routines could be useful in producing desirable materials for high-temperature applications, provided the relationship between the grain boundary network characteristics and creep properties is first established.

The structure-property relationships of the heterogeneous grain boundary networks are often simplified by using a binary classification scheme for the grain boundary character. For example, high coincidence boundaries often exhibit "special" properties such as dramatically lower diffusivities[11] and sliding rates[12,13] as compared to other more "general" boundaries. As these properties directly impact high-temperature creep, a number of investigators[4–7] have sought to experimentally correlate creep properties with simplified measures of the GBCD, e.g., the total fraction of special grain boundaries, p. Lehockey and Palumbo[4] found that an increase in p from 13% to 66% reduced the creep rate of Ni by a factor of 16 at 723 K. Thaveeprungsriporn and Was[5] increased p from 16% to 35% in Ni-16Cr-9Fe and found that the creep rate at 633 K decreased by a factor of about 26 and 66 for grain sizes 330 and 35 μm, respectively. In a study on austenitic stainless steel, a grain boundary engineered alloy with $p \approx 63\%$ exhibited creep rates (at 923 K) more than 2 orders of magnitude lower than the same alloy with $p < 25\%$.[7] These experiments are all carried out under different conditions, but they consistently indicate that special boundaries are more resistant to creep deformation than general boundaries. However, the available experimental data are very sparse, and a systematic understanding of the effect of special boundaries for specific creep deformation mechanisms, and over the full range of p, is not yet available.

One existing model that describes the creep rate of a polycrystal as a function of the special boundary fraction focuses on dislocation creep.[5] This model is based on the assumption that special boundaries inhibit dislocation motion and that dislocation annihilation can only occur if at least two of the boundaries meeting at a triple junction are general boundaries. One difficulty with applying this model is that the requirement for dislocation annihilation in grain boundaries of various types remains unclear presently. In contrast, the diffusion properties of grain boundaries have been intensively studied and are generally well understood.[11,14,15] A more tractable problem therefore might be to first study the effect of the GBCD on diffusional creep.

Creep deformation can occur by diffusional transport at very low stress levels, and as first proposed by Coble,[16] the required mass redistribution can be accomplished solely by stress-induced grain boundary diffusion. Since the grain boundary diffusivity is determined by the specific grain boundary structure, Coble creep strongly depends on the grain boundary character distribution. Tong *et al.*[17] simulated Coble creep of a general boundary honeycomb network characterized by diffusivity D_g containing a single special boundary with diffusivity $D_s = 0.8D_g$, and showed that a subtle stress concentration develops at this special boundary. For the same system, Moldovan *et al.*[18] further demonstrated that the stress localization is more pronounced as D_s decreases; the local stress is enhanced by a factor of 2.25 for $D_s = 0.01D_g$. Interestingly, the opposite case of a special boundary network containing a single general boundary does not yield a quantitatively symmetric state: the local stress is decreased only by 50%.[18] This asymmetry suggests that special boundaries play a more significant role in determining the stress distribution than do the general boundaries. Asymmetry between the role of special and general boundaries has also been observed in terms of deformation homogeneity.[19]

While introducing a general boundary into a special boundary network does not disturb the deformation pattern very much, the presence of a special boundary in a general boundary network substantially breaks the deformation regularity in its vicinity. In short, all previous work on dilute binary networks has revealed that variations in grain boundary character lead to nontrivial stress or deformation localization during Coble creep. Even more pronounced effects can be expected for networks away from the dilute limit as grain boundaries coordinate with each other in a more complicated way.

In a recent paper,[20] we studied Coble creep of a randomly distributed binary (special/general) grain boundary network over the full range of special boundary fraction. We observed that the creep viscosity exhibits a percolation threshold about 0.11 lower than the geometric connectivity threshold for special boundaries. In other words, the system begins to creep like a network of special grain boundaries well before there is a geometrically connected path of such boundaries across the structure. This result speaks to strong correlations among grain boundaries imposed by the physics of creep. In this paper, we substantially expand upon our work in Ref. 20 and present quantitative correlation and percolation analysis for Coble creep of both randomly distributed and crystallographically consistent grain boundary networks in two dimensions. The correlations are revealed across both small and large length scales using numerical simulations. We also examine the evolution of the energy dissipation in the creeping system across the percolation threshold and explore the possibility of energy redistribution being the physical origin of the percolation transition. Some other interesting percolation phenomena observed in the creeping system are also discussed.

II. SIMULATION METHOD

The simulation procedures used in this work are essentially similar to those of Hazzledine and Schneibel[21] and Ford *et al.*,[22] and were briefly described in our previous letter.[20] In this section, we mainly provide additional details regarding the setup of the problem and the important assumptions.

The simulation cell is a two-dimensional honeycomb lattice covering a nearly square domain of size 105×104 (in units of grain boundary length), which contains 4331 grains and 12 730 grain boundaries. The grain boundaries are classified into two types: general boundaries of a high diffusivity D_g and special boundaries of a low diffusivity D_s. D_g/D_s is referred to throughout as the diffusivity contrast ratio. These two types of boundaries are distributed on the honeycomb network either randomly or in such a way as to form the series of crystallographic textures described as a "fiber texture" family in Ref. 23. Comparison between the two categories of networks is made to distinguish between the correlations intrinsic to the creep process and the correlations imposed by the crystallographic constraints present in true polycrystals. The incorporation of physically meaningful correlations in the GBCD is also a necessary first step for understanding creep in realistic grain boundary engineered microstructures.

We perform uniaxial creep simulations under a constant strain rate condition and focus on the response at zero strain. The top and bottom grains in the simulation cell are assigned a prescribed and a zero vertical velocity, respectively, and the side grains are constrained to move at the same horizontal velocity so as to preserve the rectangular shape of the system. Such velocity boundary conditions lead to more accurate and reliable numerical results as compared to those obtained under other (i.e., stress-type) boundary conditions.[22] The applied external stress is calculated as the average of the stress acting on an arbitrary cross section. The ratio of this external stress to the imposed strain rate is the creep viscosity η, which is a measure of the resistance to creep. Thus, the goal of the numerical procedure is basically to solve for the stress distribution in the system.

We assume free grain boundary sliding so that shear stress along the grain boundaries is relieved instantaneously. The normal stress σ varies along a boundary, inducing a diffusional flux J:

$$J(s) = \frac{D_{gb}}{KT} \frac{1}{L_{gb}} \frac{\partial \sigma}{\partial s}, \tag{1}$$

where D_{gb} is the grain boundary self-diffusivity and is equal to D_g or D_s depending on the assigned grain boundary character, L_{gb} is the grain boundary length, s is a unitless path coordinate ranging from 0 to 1 along a boundary, K is Boltzmann's constant, and T is the absolute temperature. The normal stress σ is positive if it is tensile, negative if compressive. The atomic flux J is not uniform along the boundary. As a result, some diffusant in the boundary has to absorb onto the neighboring grains, or some matter in the lattice has to enter the boundary, at a rate

$$V(s) = -\frac{\delta \Omega D_{gb}}{KT} \frac{1}{L_{gb}^2} \frac{\partial^2 \sigma}{\partial s^2}, \tag{2}$$

where δ is the grain boundary width and Ω is the atomic volume. We assume that matter leaves or enters equally on both sides of the boundary and that no overlap or void forms as a result of the plating process. Thus, adjacent grains have to separate or approach each other at the speed V, and also rotate with respect to each other with a rate $\partial V/\partial s$. As the grains are assumed to be rigid, $\partial V/\partial s$ should be constant along the boundary, which, according to Eq. (2), requires the normal stress σ to be a cubic function of s:

$$\sigma(s) = \alpha_3 s^3 + \alpha_2 s^2 + \alpha_1 s + \alpha_0. \tag{3}$$

Here, the coefficients α_i, $i=1-4$, are all in units of Pa and are unique for every grain boundary in the system. These stress coefficients, together with the translational and rotational velocities for every grain, are simultaneously obtained as the solution to a sparse linear system of equations. In addition to the boundary conditions stated above, these equations are built upon requirements of stress continuity and flux conservation at internal triple junctions, zero flux at the grain boundary/surface intersections, mechanical equilibrium, and deformation compatibility.[21,22]

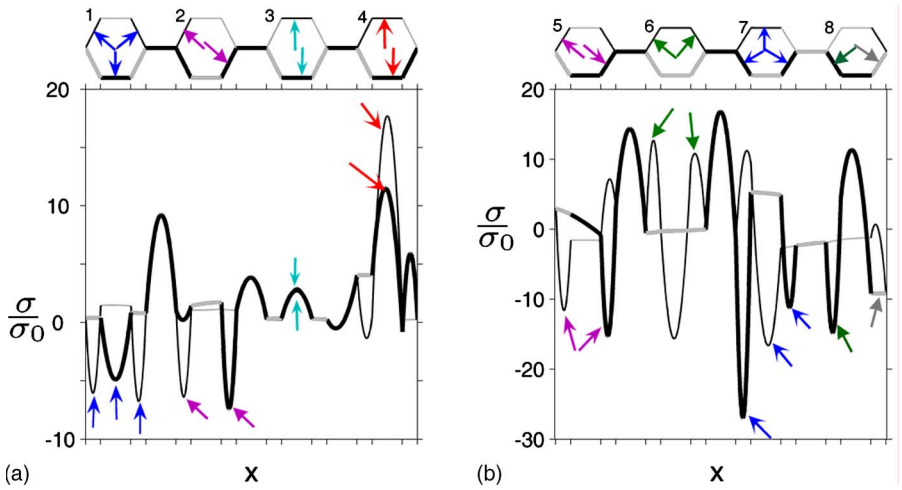

FIG. 1. (Color online) The distribution of stress σ, normalized by the external stress σ_0, along two chosen paths (a) and (b) in a random grain boundary network. The diffusivity ratio between general (in gray) and special (in black) boundaries is $D_g/D_s=10^4$, and the special boundary fraction is $p\approx 0.5$. The thickness distinguishes the two paths (upper and lower) in each figure. The arrows point out stress concentrations and correlations as described in the text.

After the stress coefficients α_i are determined, the stress σ, the diffusional flux J, and the plating rate V along each grain boundary can then be directly obtained from Eqs. (1)–(3). The distributions and correlations of these quantities will be analyzed in Sec. III. In addition, we calculate the external stress σ_0 by averaging the stress across the top surface of the simulation cell and obtain a creep viscosity η for each network configuration of special boundary fraction p. The expression of η as a function of p reduces to a typical percolation problem or a composite problem. Thus, we shall use both percolation methods and empirical effective-medium composite schemes to study the dependence of Coble creep on the GBCD in the subsequent sections.

III. CORRELATION ANALYSIS

A. Stress concentration due to the GBCD

During Coble creep, the internal stress distribution in the system is nonuniform due to variations in the grain boundary diffusivities, as well as topological heterogeneities such as a distribution of grain sizes or grain shapes.[24] It has been shown that the local stress enhancement at grain boundaries arising from a diffusivity variation is significantly higher than that caused by geometric irregularities.[18] While the presence of a single large grain yields a peak stress about $2.7\sigma_0$, introducing a single special boundary into a honeycomb network with a diffusivity contrast ratio of 10^2–10^4 results in a concentrated stress as high as $4.6\sigma_0$.[18] We have observed even greater stress concentrations in the more general case where the two types of grain boundaries are randomly distributed in the network.

Figures 1(a) and 1(b) show the distribution of stress, normalized by the external stress σ_0, along some selected paths in a random grain boundary network, which contains ~50% special boundaries ($p\approx 0.5$) with a diffusivity contrast ratio $D_g/D_s=10^4$. Both paths are perpendicular to the applied stress (strain) axis and lie in the middle of the sample. Special boundaries are in black and general ones are in gray, while the thickness of the boundaries distinguishes the upper and lower paths in each of the two figures. The first important point observed in Fig. 1 is that the local normal stress along grain boundaries can be enhanced relative to σ_0 by a factor of about 20 or higher, for both tensile stress as in Grain 4 and compressive stress as in Grain 7. In the present simulations, no relaxation mechanisms beyond diffusion are allowed, but such pronounced stress concentrations could certainly facilitate crack or cavity nucleation. Interestingly, though, the worst stress concentrations mostly occur at special boundaries which are usually resistant to crack propagation. A second observation in Fig. 1 is that, compared to a single species network where all horizontal boundaries (boundaries perpendicular to the stress axis) share the same distribution of tensile stress and all lateral boundaries also have the same distribution of mostly compressive stress,[21,22,25] the presence of a second species not only modifies the magnitude of the stresses but can also sometimes change the sign of the stresses. For example, stresses along the horizontal special boundary (in black) in Grains 1, 6, and 7 become compressive, and stresses along the top lateral special boundary in Grain 7 become tensile. A third message Fig. 1 delivers is that there is a strong correlation between the stress distributions of either two opposing grain boundaries in the same grain, such as the boundaries marked by the arrows in Grains 2–5, or two or three second-nearest-neighbor boundaries, such as the marked boundaries in Grains 1 and 6–8.

All these stress distribution irregularities and correlations can be explained by the imposed mechanical equilibrium. Force balance across the grain is most easily realized by balancing the stresses on opposing grain boundaries, as is the case for Grains 2–5. This is especially true when both of the opposing boundaries are special boundaries, which are more effective at carrying stress and are, in fact, the stress concentrators in the network. Another well balanced boundary distribution is where three special boundaries form a tripodal arrangement in a grain, such as in Grains 1 and 7. In this case, these three special boundaries often adopt similar stress distributions in order to achieve force equilibrium; this is also why the stresses along the horizontal special boundaries in Grains 1 and 7 are compressive instead of being tensile, as would be typical for horizontal boundaries. A less common but also effective way of balancing the force across a grain is exhibited in Grains 6 and 8, where two second-nearest-

neighbor boundaries share similar stress distributions. It is worth mentioning that although stress concentration mostly occurs at special boundaries, occasionally general boundaries, such as that marked by a gray arrow in Grain 8, can have a high stress as well.

While Figs. 1(a) and 1(b) provide strong evidence for correlations among grain boundary stresses, they are only specific examples of two small regions from a much bigger system. Inspection over the whole system is made possible using a spatial correlation function in what follows.

B. Correlations among boundary stresses

Integration of the normal stress $\sigma(s)$ in Eq. (3) over the range $0 \leqslant s \leqslant 1$ yields the average stress exerted on a grain boundary. Because all boundaries in the network have the same length, this is essentially a force F. We choose the center of a boundary to define its position $\vec{r}_0$ in the network, and define the spatial autocorrelation function among boundary forces as

$$R(r) = \frac{\sum_{\vec{r}_0,\vec{r}_0+r} (F_{\vec{r}_0} - \bar{F})(F_{\vec{r}_0+r} - \bar{F})}{\sqrt{\sum_{\vec{r}_0,\vec{r}_0+r} (F_{\vec{r}_0} - \bar{F})^2} \sqrt{\sum_{\vec{r}_0,\vec{r}_0+r} (F_{\vec{r}_0+r} - \bar{F})^2}}, \quad (4)$$

where $\bar{F}$ denotes the average F for all boundaries in the system, and $\vec{r}_0+r$ denotes each boundary a distance r away from the boundary centered at $\vec{r}_0$. It is important to note that $R(r)$ is calculated from all appropriate pairs of two boundaries r distance apart from each other, regardless of their positions in the system and their orientations with respect to the external stress axis. $R(r)$ equals +1 if the forces on two boundaries r distance away from each other always covary positively and perfectly, −1 if they covary negatively and perfectly, and zero if they vary independently.

We first calculate the correlation coefficient $R(r)$ for the forces acting on two boundaries in the same grain. The sign and magnitude of R calculated this way characterize the frequencies of the force balance types shown in Fig. 1 and indicate how the force equilibrium is, on average, achieved in the system. The diffusivity contrast ratio D_g/D_s is fixed at 10^4, while the special boundary fraction p covers the full range 0–1. The obtained R values are plotted in Fig. 2 for all the three possible distances between two boundaries in the same grain, $r=\sqrt{3}$, 1.5, and $\sqrt{3}/2$ (in units of grain boundary length).

In Fig. 2, the data for $r=\sqrt{3}$ correspond to force transmission across two opposing boundaries in a grain (such as the cases of Grains 2–5 in Fig. 1). Three points can be made from this set of data. First, R for $r=\sqrt{3}$ is higher than 0.5 over the full range of special fraction p (except for a few outlying data points). This is consistent with the observation in Fig. 1 that force balance on opposing boundaries is the major mode of force equilibrium of a grain. The limiting cases at $p=0$ and 1 present the extremes of this trend: the force balance in homogeneous networks is completely accomplished across opposite sides of the grain, leading to $R=1$. Second, R for $r=\sqrt{3}$ shows an opposite trend with p to that for $r=1.5$; as

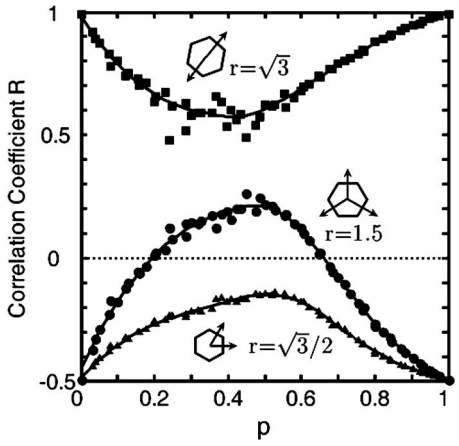

FIG. 2. Correlation coefficient R [Eq. (4)] of the grain boundary forces as a function of the special boundary fraction p for the distances $r=\sqrt{3}/2$, 1.5, and $\sqrt{3}$ (in units of grain boundary length). All three of these distances correspond to those connecting boundaries on the same grain in the configurations shown by the inset diagrams.

the network becomes more heterogeneous, the lines of force transmission are more often deflected by the force balance between second-nearest-neighbor boundaries. Third, R for $r=\sqrt{3}$ is asymmetric with respect to $p=0.5$, for example, being higher at $p=0.8$ than at $p=0.2$. We believe that this asymmetry reflects special boundaries being more effective at transmitting forces.

In Fig. 2, R values for $r=1.5$ are negative when the fraction of special boundaries $p<0.2$ or $p>0.65$ and become positive in between; from this, we may state that tripodal force balance among second-nearest-neighbor boundaries across a grain becomes effective for $p \approx 0.2$–0.65. This is understandable based on the types of force balance seen in Grains 1 and 6–8 in Fig. 1. As p approaches 0.5, the probability of having a force balance (similarity) among three special boundaries forming a tripodal configuration or among only two second-nearest-neighbor boundaries increases, and the correlation coefficients correspondingly increase above zero. R values for $r=\sqrt{3}/2$ are always negative, which means that the nearest-neighbor boundaries tend to have dissimilar stresses or forces.

We have also calculated the correlation coefficient $R(r)$ including all possible pairs of grain boundaries r distance apart from each other, without restricting both boundaries to be from the same grain. For $r=1.5$ and $\sqrt{3}/2$, this procedure is the same as the previous calculation in Fig. 2 because all possible pairs of boundaries at these two distances always belong to the same grain. For $r=\sqrt{3}$, however, this procedure includes numerous other configurations with the same characteristic separation, in addition to the case of two boundaries on opposite sides of a grain; for example, the distance $\sqrt{3}$ marked by the dashed arrows in Fig. 3(c) does not correspond to a straightforward force transmission path across a grain, but it is also included in the calculation. In fact, all distances of $r \geqslant \sqrt{3}$ correspond to boundary pairs with more than one configuration [some are shown in Fig. 3(c)]. By averaging over all the possible configurations, the correlation

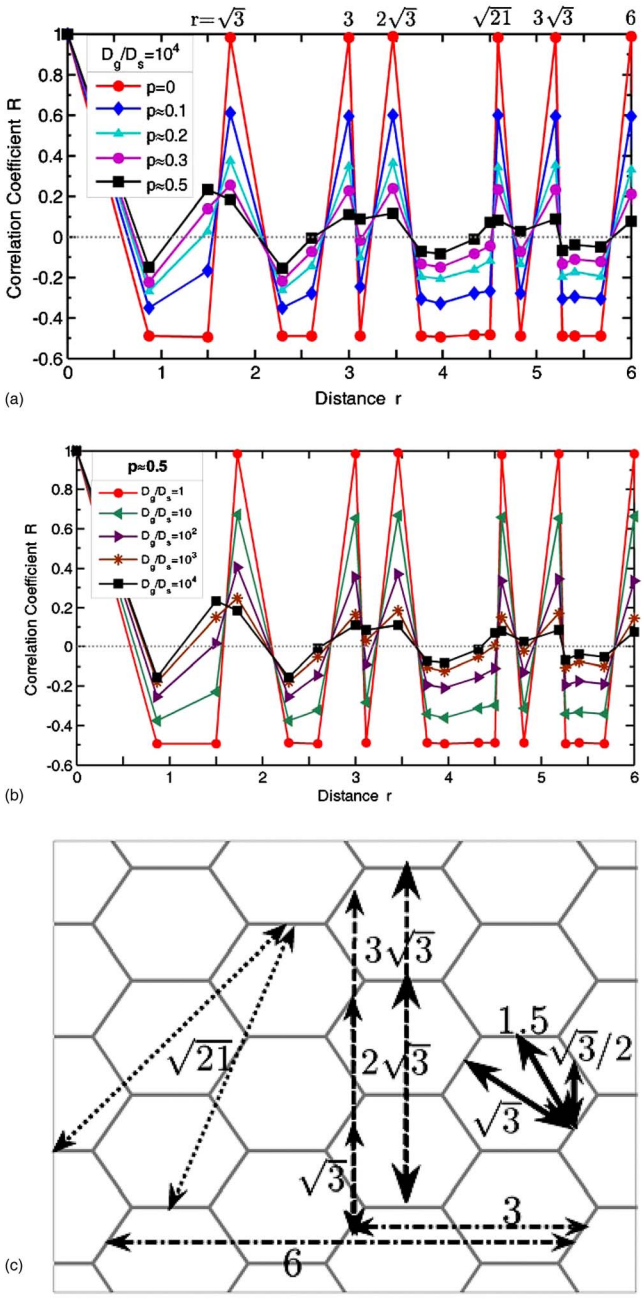

FIG. 3. (Color online) Correlation coefficient R [Eq. (4)] of the grain boundary forces as a function of the distance r (in units of grain boundary length). R is computed for five special boundary fractions $p=0$, $p\approx0.1$, 0.2, 0.3, and 0.5 under a diffusivity ratio $D_g/D_s=10^4$ in (a) and for diffusivity ratios $D_g/D_s=1$, 10, 10^2, 10^3, and 10^4 at a special fraction $p\approx0.5$ in (b). Examples of the various paths are illustrated in (c).

coefficients R for these large distances at a certain p simply represent the degree of disorder in the force distribution, i.e., how much the regular force distribution on a homogeneous network has been disturbed by the random distribution of the boundary character. The remaining discussion in this section will focus on distances $r\geqslant\sqrt{3}$.

Figure 3(a) plots $R(r)$ for r from 0 to 6, which includes the 19 nearest neighbors, for a diffusivity contrast ratio $D_g/D_s=10^4$. The five curves correspond to networks with different special boundary fractions, $p=0$, 0.1, 0.2, 0.3, and 0.5. The condition $p=0$ corresponds to a homogeneous network exclusively composed of one type of grain boundary, in which the force distribution exhibits perfect positive correlation ($R=1$) for $r=\sqrt{3}$, 3, $2\sqrt{3}$, $\sqrt{21}$, $3\sqrt{3}$, and 6. These specific separations all correspond to distances between two parallel boundaries, as illustrated in Fig. 3(c). At $p=0$, the forces on all horizontal boundaries are the same, and all lateral boundaries also have the same force. Thus, two parallel boundaries, both horizontal or both tilted, always share the same stress distribution and force. Meanwhile, two nonparallel boundaries must comprise a pair of either horizontal and tilted or right-tilted and left-tilted boundaries; the probability of the former combination is higher than that of the latter, and therefore the forces on two nonparallel boundaries are more often dissimilar, resulting in a negative correlation coefficient for many distances.

For binary networks, the values of R at all distances $r\geqslant\sqrt{3}$ simply indicate how reasonable it is to represent the force distribution for a binary network with the homogeneous network solution, i.e., a distribution with only two distinct values, one for all horizontal boundaries and the other for all tilted boundaries. The closer R is to zero, the worse such a simplified representation is for heterogeneous networks. As the special fraction p increases to 0.5 [Fig. 3(a)], both the positive correlations between parallel boundaries and the negative correlations between nonparallel boundaries gradually diminish; the correlation directionality gradually recovers as p keeps increasing above 0.5 (not shown in the figure). R for all distances $r\geqslant\sqrt{3}$ approaches zero as p approaches 0.5 from either below or above because the distinct difference between forces on horizontal and tilted boundaries is gradually blurred by the random distribution of the boundary character. The similar peak heights or depths for different separation distances at a certain p in Fig. 3(a) can also be explained by the nature of R. A correlation coefficient that is essentially determined by geometric orientation (the boundaries being horizontal or tilted) should be similar on different length scales.

In addition to the distribution of grain boundary character described by the special boundary fraction p, the diffusivity contrast ratio between general and special boundaries, D_g/D_s, is another parameter that controls the degree of network randomization. The effect of D_g/D_s on the force correlations is illustrated in Fig. 3(b). At $p\approx0.5$, the force distributions in networks with higher D_g/D_s ratios are more random (i.e., less directional). As D_g/D_s decreases toward unity, the correlation coefficient R exhibits sharp peaks and valleys again; the network with $D_g/D_s=1$ at any p is equivalent to a network of predominantly one boundary species.

In brief, because the requirement of force equilibrium for every grain is mandatory, strong correlations among boundary forces are manifested during Coble creep. Although special boundaries are usually the stress concentrators in the system, even for networks with randomly distributed grain boundary character, the distribution of the average stresses (or forces) on boundaries is generally highly correlated.

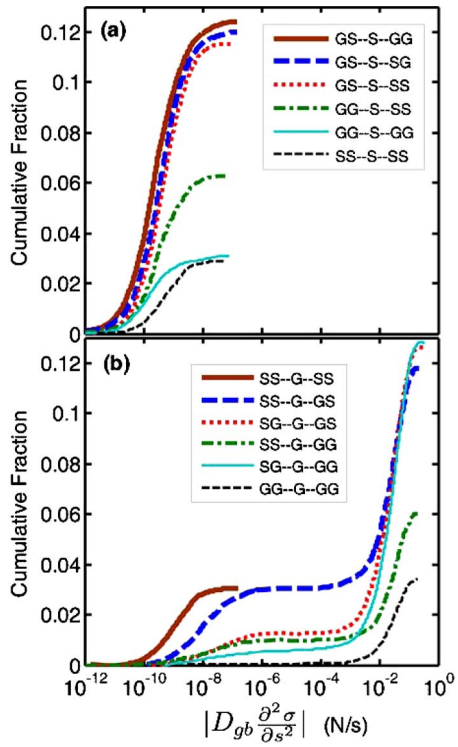

FIG. 4. (Color online) The distribution of the absolute value of the plating rate V [Eq. (2)], excluding the prefactor constants, for a boundary in different surroundings. The data for special boundaries with different nearest neighbors are plotted in (a) and general boundaries in (b). "S" denotes special boundary and "G" general boundary. In this example, the network has a special boundary fraction $p \approx 0.5$ and a diffusivity ratio $D_g/D_s = 10^{10}$.

C. Plating rates of boundaries with different nearest neighbors

In the honeycomb network, the first nearest neighbors of a boundary are those meeting it at the adjoining triple junctions. Each boundary has four nearest neighbors, which serve as sources or sinks for matter flow in the boundary of interest, and therefore the characters of the four neighbors may influence the rate of matter removal or deposition at a specific boundary. The distribution of the plating rate of a boundary in different surroundings is plotted in Fig. 4, where "S" denotes a special boundary and "G" a general boundary; for example, "GS-S-SS" denotes a special boundary meeting one general and one special boundary at one triple junction, and meeting two special boundaries at the other triple junction. Figure 4 is computed for a network composed of half general and half special boundaries ($p \approx 0.5$), where the diffusivity contrast has been increased to 10^{10} in order to make the correlation effect evident. The x axis is the absolute value of the plating rate V [Eq. (2)] (in units of m/s) excluding the prefactor constants $\delta\Omega/KTL_{gb}^2$ [in units of $1/\mathrm{m\,Pa}$], and therefore the x-axis labels are in units of N/s; the y axis is the cumulative fraction of boundaries exhibiting that rate. Each curve corresponds to a different neighborhood. The data for special boundaries with different neighbors are plotted in Fig. 4(a), and those for general boundaries in Fig. 4(b).

In Fig. 4(a), special boundaries surrounded by different neighbors have quite similar average plating rates, which are generally distributed on the range 10^{-12}–10^{-7}. Special boundaries have a much lower diffusivity than general boundaries and are the plating rate-limiting species in the system. It therefore seems reasonable that the plating rates of special boundaries do not depend very much on the character of neighboring boundaries. In contrast, the average plating rate of a general boundary is substantially impacted by its surroundings [Fig. 4(b)]. The general boundaries with four general boundary neighbors ("GG-G-GG") have very high plating rates above 10^{-3}, while those surrounded by four special boundaries ("SS-G-SS") all have very low plating rates below 10^{-7}, of similar magnitude to the plating rates of special boundaries [see Fig. 4(a)]. Special boundaries are poor conduits [Eq. (1)] and are less active in exchanging matter with the grains [Eq. (2)]. They generally cannot provide sufficient matter to accommodate fast plating at their neighboring general boundaries. In other words, general boundaries surrounded by four special boundaries have low plating rates because they lack available sources or sinks for diffusion; their neighborhood coerces them to exhibit apparently special behavior.

The plating rates of other general boundaries almost all show a bimodal distribution. Take, for example, the case of a general boundary surrounded by one general and three special boundaries, labeled as "SS-G-GS." In this family of general boundaries, the plating rates of some boundaries are below 10^{-7} and others are above 10^{-3} with almost none in between. Those with plating rates above 10^{-3} are likely connected to a fairly large cluster of general boundaries by their single general neighbor; those with plating rates below 10^{-7} are probably part of a very small cluster of general boundaries, bounded by special boundaries at the second- or further-nearest-neighbor level.

To this point, we have explored the strong correlations in the creeping system in terms of both the stress (force) and plating rate distributions. Because the network configuration is not fixed and varies with the special boundary fraction, these correlation effects can only be directly revealed for a few example network configurations or over limited length scales. However, correlations have a pronounced effect on percolation phenomena; in the following, we turn our attention to an analysis of the percolation transition, which permits examination over large length scales for all values of p.

IV. PERCOLATION

A basic percolation problem studies the geometric phase connectivity of a binary system as a function of the fraction of one element type, p. When p is low, there are only small clusters of these elements in the system; when p increases to a critical value p_c, a sample-spanning cluster emerges. The geometric percolation threshold $p_c \approx 0.653$ for a honeycomb bond lattice and $p_c \approx 0.357$ for a triangular bond lattice.[26] In terms of material properties, additional percolation thresholds may be defined as the critical phase fractions at which the property-controlling species switches from one to the other. Simple transport properties such as diffusion usually have the same percolation threshold as the geometric percolation transition for the same lattice.[27] More complex me-

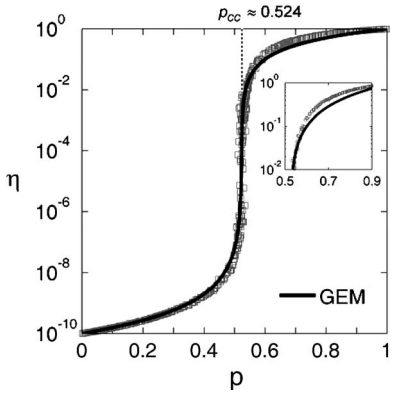

FIG. 5. The normalized creep viscosity η as a function of the special boundary fraction p for a diffusivity ratio $D_g/D_s=10^{10}$. The curve clearly shows a sharp increase at the percolation threshold $p_{cc}\approx 0.524$. The square points are the simulation data, and the solid line is the prediction of the GEM equation [Eq. (9)] discussed in Sec. V.

chanical properties, however, usually exhibit different threshold values; for example, the elastic rigidity percolation on the triangular bond lattice has a percolation threshold of ~ 0.58.[28] For Coble creep, we identified in our earlier letter[20] a percolation threshold different from all those mentioned above and a unique set of scaling exponents. Here, we provide some deeper analysis of the scaling properties and further discuss the possible underlying physics behind the unique percolation behavior of Coble creep.

A. Percolation threshold and scaling properties

The percolation threshold for Coble creep on a two-dimensional honeycomb network is $p_{cc}\approx 0.524$ for the present network size ($L\approx 104$) and extrapolates to ~ 0.542 for an infinite lattice.[20] In Fig. 5, the creep viscosity η, which has been normalized with respect to the viscosity of a network of special boundaries, is computed as a function of the special boundary fraction p for a diffusivity ratio $D_g/D_s=10^{10}$. Such a high ratio is used to clearly reveal the percolation transition—the sharp increase in η at p_{cc}, above which the binary grain boundary network has a similar viscosity to that of a network of special boundaries. The difference between p_{cc} and the geometric percolation threshold on the same lattice, $p_c\approx 0.653$,[26] can be qualitatively understood from the correlation analysis presented in Sec. III C. Because a general boundary behaves like a special boundary with a certain probability that depends on its neighborhood, the fraction of boundaries that physically serve as special ones is higher than p, the true fraction of special boundaries. This is not meant to imply that the magnitude of p_{cc} should be quantitatively attainable by comparing the fraction of specially behaving boundaries to the geometric threshold p_c. As discussed in Ref. 20, Coble creep may stand alone as a new class of percolation problem.

The scaling of the creep viscosity η with respect to the special fraction p below and above the percolation threshold p_{cc} is

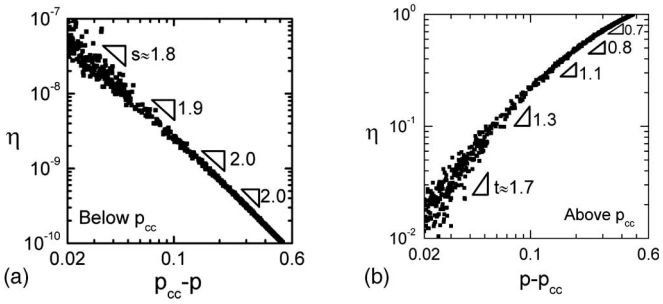

FIG. 6. The power-law scaling [Eq. (5)] of the creep viscosity η (a) below and (b) above the percolation threshold p_{cc} for a diffusivity ratio $D_g/D_s=10^{10}$. A series of local slopes is denoted on the curves.

$$\eta(p) \propto (p_{cc}-p)^{-s} \quad \text{for } p < p_{cc} \tag{5a}$$

$$\eta(p) \propto (p-p_{cc})^{t} \quad \text{for } p > p_{cc}. \tag{5b}$$

In the vicinity of the threshold, i.e., in the range $|p-p_{cc}| \leqslant 0.1$, our simulation data can be fitted with approximate asymptotic exponents of $s\approx 1.88$ and $t\approx 1.69$, as we reported in Ref. 20. The scaling relationships over the full range of p are shown in Figs. 6(a) and 6(b), where a series of local slope measurements is presented. Below the percolation threshold p_{cc}, the curve in Fig. 6(a) generally has a well defined slope close to the asymptotic value around $s\approx 1.9$. As p approaches p_{cc} from below, s slightly decreases because the creep viscosity η below and above p_{cc} have to reconcile with each other at the threshold.

In contrast, as p increases from the percolation threshold p_{cc} to 1 [Fig. 6(b)], the scaling exponent t decreases substantially from ~ 1.7 to ~ 0.7. This large variation of t is well beyond what might be expected from the normal difference between near-threshold and far-from-threshold behaviors. For example, the drift is only about 0.1–0.2 for s in Fig. 6(a), and even less than that in the simpler problem of concentration-gradient-driven diffusion; in that case, the problem is governed by the geometric connectivity, and t is nearly a constant over the full range of p above the percolation threshold.[27] Here, the decrease in t indicates that the effect of introducing a special boundary into the network is more significant at higher p. The reason might be that the strong physical creep correlations among the grain boundaries are affected by the geometric connectivity, which varies as p increases.

B. Distribution of the energy dissipation

As an atom diffuses down the chemical potential gradient, the work done on the atom is finally dissipated as heat. Because we have assumed free grain boundary sliding, i.e., shear stress is relieved instantaneously and performs no work, the supplied external work is all dissipated via diffusion along the grain boundaries. The rate of energy dissipation in one boundary E is

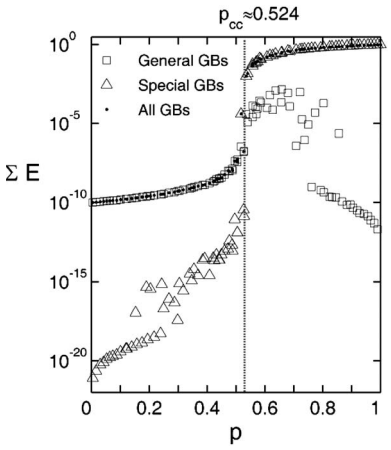

FIG. 7. Summations of the dissipated energy E [Eqs. (6)–(8)] over all general boundaries, all special boundaries, and all the grain boundaries in the network, for a contrast ratio $D_g/D_s=10^{10}$. ΣE values have all been normalized with respect to $(\Sigma E)_{p=1}$.

$$E = \frac{\delta L_{gb}}{\Omega}\int_0^1 \frac{KT}{D_{gb}}\Omega^2 J^2 ds, \tag{6}$$

with the diffusional flux J defined in Eq. (1). Thus, E can be rewritten as

$$E = \frac{\delta\Omega D_{gb}}{KTL_{gb}}\int_0^1 \left(\frac{\partial\sigma}{\partial s}\right)^2 ds. \tag{7}$$

The stress σ is given by the cubic function in Eq. (3), and therefore Eq. (7) becomes

$$E = \frac{\delta\Omega D_{gb}}{KTL_{gb}}\left(\frac{9}{5}{\alpha_3}^2 + 3\alpha_3\alpha_2 + 2\alpha_3\alpha_1 + \frac{4}{3}{\alpha_2}^2 + 2\alpha_2\alpha_1 + {\alpha_1}^2\right). \tag{8}$$

The rate of energy dissipation E in Eq. (8) has the unit of J/(m s) in two dimensions. The multiplicative prefactors $\delta\Omega/KTL_{gb}$ (in units of 1/Pa) have been neglected in the present calculation, and thus the E values reported here are all in units of $Pa^2\ m^2/s$.

In Fig. 7, we show the summations of E over all general boundaries, all special boundaries, and all the grain boundaries in the network, for a contrast ratio $D_g/D_s=10^{10}$. The ΣE values have all been normalized with respect to $(\Sigma E)_{p=1}$. The summation of E over all the grain boundaries is equal to the external work, which is proportional to the creep viscosity η under constant strain rate conditions. Therefore, the dotted curve in Fig. 7 is of the same shape as the η curve in Fig. 5 and also reveals the same percolation transition point p_{cc}. However, in Fig. 7, we now see the basic physical shift that underlies the percolation transition. Below p_{cc}, energy is dissipated predominantly in general boundaries, and the energy dissipation in special boundaries is trivial, while above p_{cc}, energy dissipation mainly takes place in special boundaries. An interesting secondary observation pertains to the two trivial contributions, which each exhibit additional discontinuities. The trivial dissipation in special boundaries has a discontinuous jump around $p\approx 0.15-0.3$, while in the general boundaries, a similar discontinuity occurs at $p\approx 0.75-0.85$. The origin of these unusual secondary discontinuities is not clear but might be related to a change of the role of the dilute species in the network: the possibility of stress or deformation concentration decreases as p approaches the dilute limits of 0 or 1.

As E in Eq. (8) represents each boundary's contribution to the overall energy dissipation, the distribution of E reflects the behavioral heterogeneity in the network. Histograms of E for general boundaries and for special boundaries are, respectively, plotted in Figs. 8(a) and 8(b) at several special fractions below and above the percolation threshold ($p_{cc}\approx 0.524$). For general boundaries [Fig. 8(a)], as p approaches p_{cc} from below (dashed curves), the distribution shifts to the right, and the primary peak reduces in height. The distribution even becomes bimodal for the case of $p\approx 0.522$ plotted with the red dashed line; above p_{cc}, the distribution peak shifts back to the left as p increases, suggesting a decrease in the energy dissipated in general boundaries. For special boundaries [Fig. 8(b)], we see the opposite situation. The distribution is broadened and shifted to the right as p increases below p_{cc} (dashed curves), and becomes bimodal right above p_{cc} (solid curves); as p further increases, the peak corresponding to low energies gradually diminishes while the other peak at higher energies grows in magnitude and shifts to the right. This is consistent with Fig. 7 which shows that as p increases above p_{cc}, more energy is dissipated in special boundaries.

To better compare between general and special boundaries, we have normalized the E value of every boundary with respect to the average energy dissipation rate of a boundary, $\bar{E}$, at the specific p value and plot the normalized histogram of $E/\bar{E}$ for general boundaries in Fig. 8(c) and for special boundaries in Fig. 8(d). There are striking similarities between the distribution of $E/\bar{E}$ for general boundaries below p_{cc} [dashed lines in Fig. 8(c)] and that for special boundaries above p_{cc} [solid lines in Fig. 8(d)]. Firstly, the main histogram peak is always centered around $E/\bar{E}=1$, which confirms that the main energy dissipation species is general boundaries below p_{cc} and special boundaries above p_{cc}. Secondly, as p approaches p_{cc} from below for general boundaries and from above for special boundaries, the height of the main peak decreases, and meanwhile, a second peak emerges and grows at much lower $E/\bar{E}$ values. This near-threshold bimodal distribution for both species will be further explored in Sec. IV C. The single peak for general boundaries above p_{cc} [solid lines in Fig. 8(c)] and that for special boundaries below p_{cc} [dashed lines in Fig. 8(d)] exhibit similar trends as well.

C. Connectivity of the "energy backbone"

The distribution of the dissipated energy E on networks with $p\approx 0.522(<p_{cc})$ and $p\approx 0.537(>p_{cc})$ is, respectively, plotted in Figs. 9(a) and 9(c). The E values marked on the scale bar do not include the prefactor constants in Eq. (8) and have the unit of $Pa^2\ m^2/s$. In Fig. 9(a), the energy level

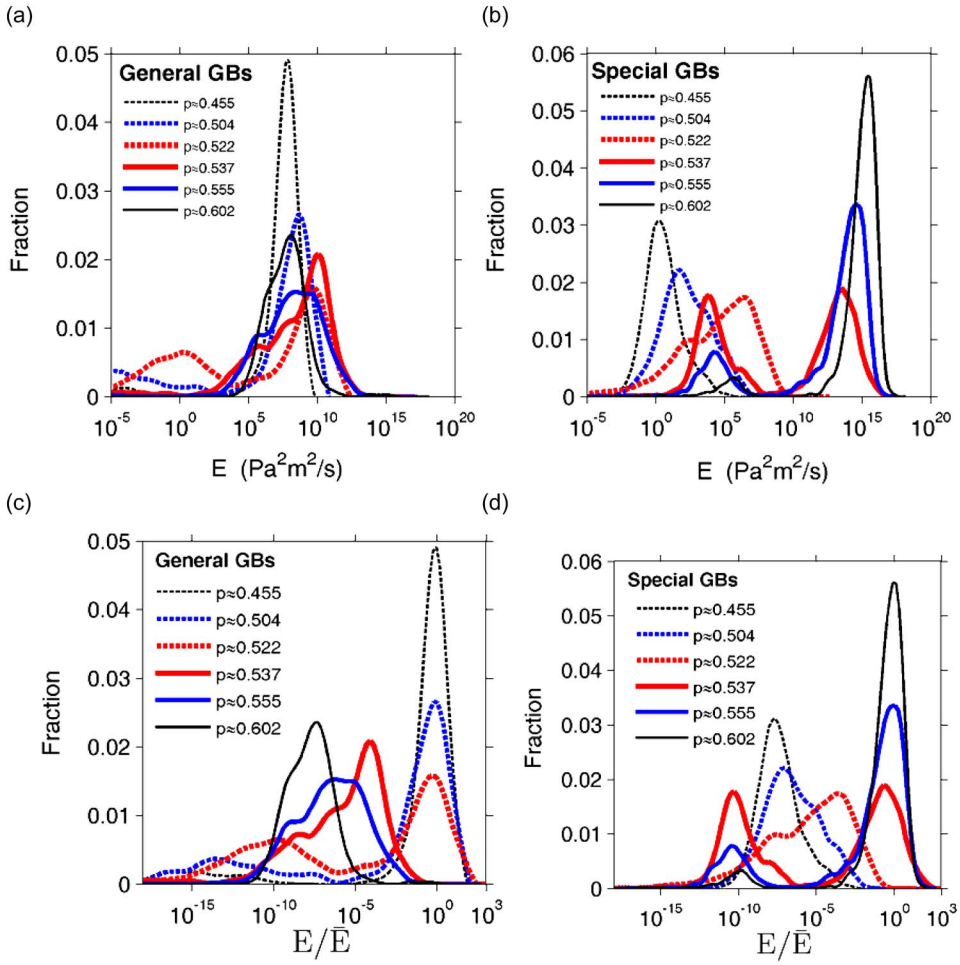

FIG. 8. (Color online) The histograms of the dissipated energy E [Eqs. (6)–(8)] for (a) general boundaries and (b) special boundaries below (dashed curves) and above (solid curves) the percolation threshold ($p_{cc} \approx 0.524$) for a diffusivity ratio $D_g/D_s = 10^{10}$. The E value of every boundary is further normalized with respect to the average energy dissipation rate of a boundary, $\bar{E}$, at the specific fraction. The histograms of $E/\bar{E}$ are plotted in (c) for general boundaries and (d) for special boundaries.

throughout the network is generally very low, in accordance with the low creep viscosity of the system below the percolation threshold p_{cc}. In Fig. 9(c), the overall E level is much higher, indicating an increase in the creep viscosity above p_{cc}. In both Figs. 9(a) and 9(c), some of the boundaries dissipate energy at a rate many orders of magnitude higher than others. Although these fast dissipating boundaries appear, at a coarse level, to connect the opposite sides of the system, they are actually not connected into a sample-spanning cluster. In fact, neither any sample-spanning cluster of general boundaries nor one of special boundaries could form for both special fractions considered in Fig. 9, as both fractions are significantly lower than the geometric connectivity threshold. Thus, the percolation transition and the dramatic change in the energy dissipation distribution are not induced by geometric connectivity on the honeycomb lattice.

There is a strong correlation between the magnitude of E for a boundary and its species. Below p_{cc}, the boundaries with relatively fast energy dissipation are mainly general boundaries and exhibit winding morphologies [dark boundaries in Fig. 9(a)]. These general boundaries dissipate energy faster mainly because of their higher diffusivity [Eqs. (6)–(8)]. Thus, the energy distribution should be correlated with the connectivity and clustering of general boundaries. This is clearly seen in Fig. 9(b) which plots the dissipated energy in all the general boundaries at $p \approx 0.522$ on the honeycomb lattice. In general, the energy dissipation rates of the general boundaries belonging to the same small cluster are either all very high or all very low.

Above p_{cc}, the boundaries with relatively fast energy dissipation are mainly special boundaries and form long chains of small rings [dark boundaries in Fig. 9(c)]. Special boundaries become the main dissipating species because of the higher stress gradients they sustain [see Eq. (7) and Fig. 1], and such higher stress gradients usually correlate with higher absolute magnitudes of the average stress or force on these boundaries. As described in Sec. III A, mechanical equilibrium of each grain is achieved by the balance of the forces among the boundaries around a grain, mainly connecting second- and third-nearest-neighbor bonds on the honeycomb lattice. Therefore, above the percolation threshold, the true connections among boundaries are not those where the boundaries meet at triple junctions but rather those defining the force network across the grains. This definition of artificial connectivity across grains corresponds to true connectivity on the dual lattice—for the honeycomb network, the dual is the triangular lattice. We can map each boundary in the honeycomb lattice onto the triangular dual lattice by assigning a dual bond connecting the center of its two adjacent grains, while keeping its species identity. The distribution of E for special boundaries at $p \approx 0.537$ on the triangular lattice is plotted in Fig. 9(d). The special boundaries with high E

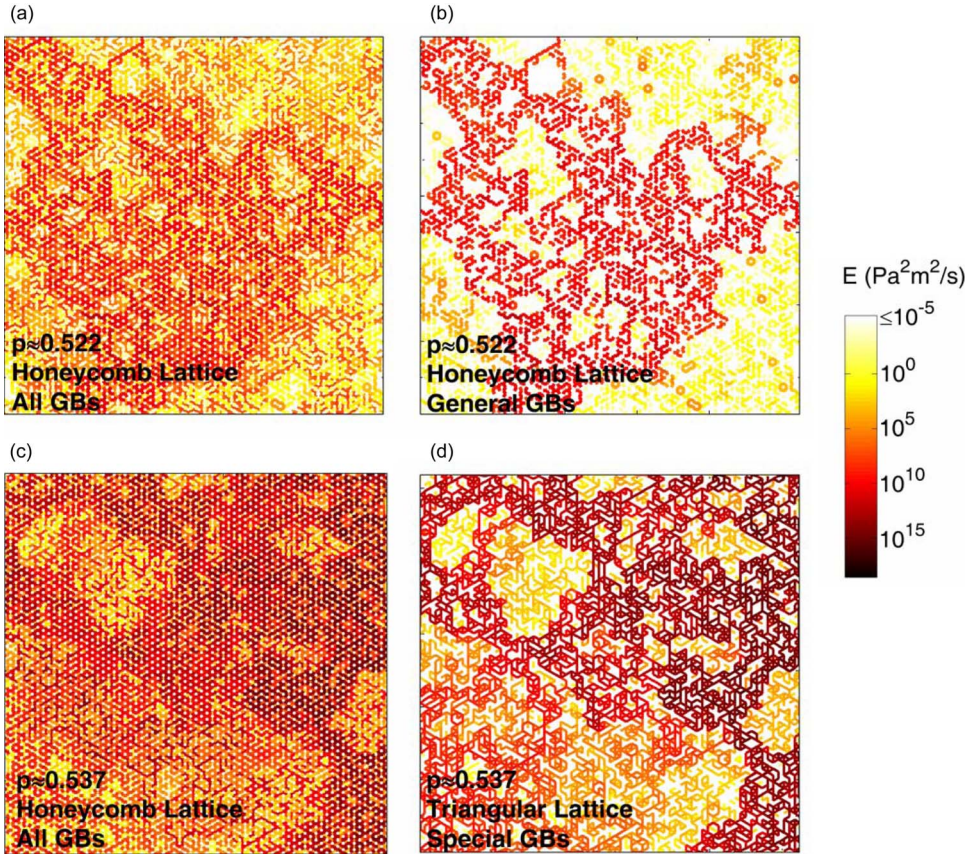

FIG. 9. (Color online) The spatial distribution of the dissipated energy E [Eqs. (6)–(8)] on the network. (a) All grain boundaries on the honeycomb lattice at the special fraction $p \approx 0.522$ (below percolation threshold). (b) Only general boundaries on the honeycomb lattice at $p \approx 0.522$. (c) All boundaries on the honeycomb lattice at $p \approx 0.537$ (above percolation threshold). (d) Only special boundaries on the triangular (dual) lattice at $p \approx 0.537$.

values in Fig. 9(d) now form a sample-spanning connected cluster. What is more, the shape of this cluster closely resembles the morphology of the rigid backbone in elastic networks,[29–31] which is in line with our assertion that force balance and transmission play an important role in the percolation transition of Coble creep.

Finally, we recall that in Fig. 8 at $p \approx 0.522$, the energy dissipated in general boundaries exhibited a bimodal distribution, and at $p \approx 0.537$, the energy dissipation in special boundaries was bimodal. Such bimodal distributions are obvious in Figs. 9(b) and 9(d). Further discussion on the energy dissipation distribution is provided in the Appendix, where we illustrate an additional energy inflection at p_{cc}, in the fraction of boundaries that expend vs absorb energy during creep.

V. EMPIRICAL EFFECTIVE-MEDIUM APPROACH

Although there are many complexities associated with the percolation transition, the calculation of the creep viscosity η of the binary grain boundary network is basically a composite problem that may also be addressed by conventional effective-medium averaging schemes. These provide a practical tool for predicting the creep behavior for a material with known GBCD and can be extended easily to more complex GBCDs that are nonbinary or nonrandom.[27] We use McLachlan's generalized effective-medium (GEM) equation[32,33] because it includes the percolation threshold and the scaling exponents. For the present creep problem, the GEM equation writes as

$$(1-p)\frac{\eta_g^{1/s} - \eta^{1/s}}{\eta_g^{1/s} + (p_{cc}^{-1} - 1)\eta^{1/s}} + p\frac{\eta_s^{1/t} - \eta^{1/t}}{\eta_s^{1/t} + (p_{cc}^{-1} - 1)\eta^{1/t}} = 0, \tag{9}$$

where η_g and η_s are the creep viscosities of the purely general boundary network and purely special boundary network, respectively. We have fitted Eq. (9) to the simulation data using p_{cc}, s, and t as adjustable parameters, and the best fits yield $p_{cc} \approx 0.524 \pm 0.003$, $s \approx 2.08 \pm 0.16$, and $t \approx 1.26 \pm 0.16$. The fitted percolation threshold and the exponent s are quite close to those obtained earlier by direct percolation analysis, while t is between the minimum and maximum values obtained from fitting to the scaling law in Fig. 6(b). As there is a large variation in t as p increases, $t \approx 1.26 \pm 0.16$ from the GEM fitting may be regarded as an appropriate average that generally reflects the creep properties for the whole range of p above the percolation threshold.

The GEM fitting result is added to Fig. 5 as the solid line. Equation (9) generally fits well to the simulation data over the full range of p. However, as shown in the inset, there is some deviation above the percolation threshold. This is because a single value of exponent t cannot accurately capture the behavior above the percolation threshold. This slight disagreement notwithstanding, Eq. (9) may be used in conjunction with the conventional Coble equation[16] to predict the creep behavior of a heterogeneous grain boundary network.

VI. CREEP OF CRYSTALLOGRAPHICALLY CONSISTENT GRAIN BOUNDARY NETWORKS

Discussions thus far have focused on Coble creep of networks with randomly distributed grain boundaries. Study of such random networks, on the one hand, benefits from the more direct comparison they present with the well-understood connectivity or conductivity percolation problems, but on the other hand, neglects important fundamental correlations in GBCD (Ref. 34) that influence connectivity and percolation in realistic microstructures. Here, we perform creep simulations on a simple fiber-textured family of microstructures,[23,35] where grain boundary characters are assigned in a crystallographically consistent manner.

The starting microstructure comprises grains of the same common orientation. Each grain is rotated about a shared axis by an angle randomly chosen between 0 and $\pi/3$. The misorientation between grains is then compared to a prescribed threshold angle ϕ. Grain boundaries with misorientation angles lower than ϕ are treated as special boundaries, and others are considered general boundaries; this technique only specifically recognizes low-angle boundaries as special, although other special misorientations can be included without changing the basic nature of the correlations that are introduced. By varying ϕ, we generate crystallographic networks of desired special boundary fractions. Although in this case classification of grain boundaries only involves the misorientation angle and thereby does not necessarily reflect the true structure-property relationship for every specific boundary, comparison of the creep properties between correlated and random networks can effectively reveal the effects of crystallographic constraints which must appear in any microstructure.

As shown in Fig. 10(a), the creep viscosity η exhibits a percolation transition at $p_{cc}^{crys} \approx 0.555$ for the crystallographic network and at $p_{cc}^{rand} \approx 0.524$ for the random network, both for the finite size network specified in Sec. II. The percolation threshold for Coble creep has shifted by an amount ~ 0.031 toward a higher fraction of special boundaries, due to correlations introduced by the crystallographic constraints. The direction of this shift is reasonable in that prior studies of both geometric connectivity[23] and diffusion[27] have shown that the above construction of the crystallographic network promotes connectivity among general boundaries. Therefore, more special boundaries are required to achieve the same creep resistance as the random network. The amount of the threshold shift, ~ 0.031, however, is slightly smaller than the shift in the geometric connectivity or diffusion problem, ~ 0.05.[23,27] The crystallographic networks may be configured in such a way that more general boundaries behave like special boundaries, as a result of the intrinsic correlations of the creep process. In other words, the effects of crystallographic correlations are apparently modified by the physical correlations of creep.

In Fig. 10(b), the creep viscosity η is fitted to the scaling laws of Eq. (5) below and above the percolation transition point p_{cc}^{crys} within the range $|p - p_{cc}^{crys}| \leq 0.1$. The scaling exponents are $s = 1.94 \pm 0.11$ and $t = 1.71 \pm 0.13$, which are consistent with the critical exponents for random networks, 1.88 ± 0.12 below and 1.69 ± 0.09 above the percolation threshold (see Fig. 6 and Ref. 20). These scaling exponents are specific to a certain class of percolation problems, and it has been observed for geometric and diffusion percolation that crystallographic constraints do not alter the percolation universality class.[27,36] The results in Fig. 10(b) conform to this notion but extend it to the percolation of Coble creep.

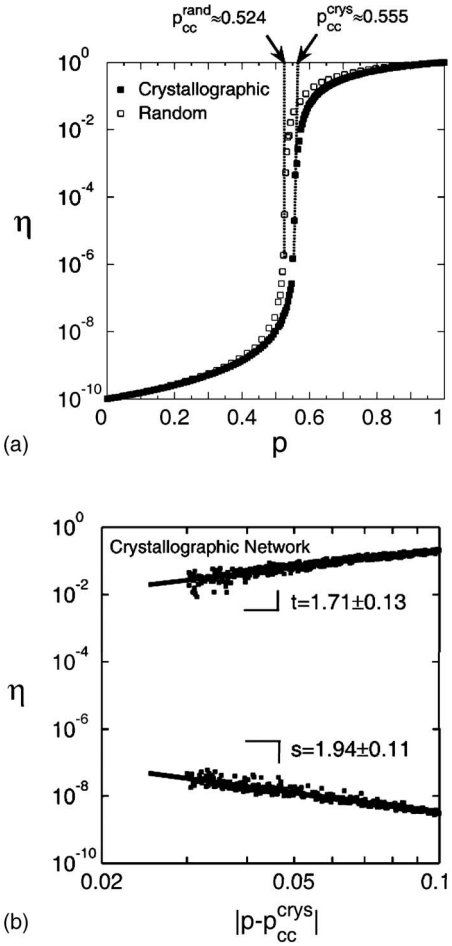

FIG. 10. (a) The creep viscosity η as a function of the special boundary fraction p. η exhibits a percolation transition at $p_{cc}^{crys} \approx 0.555$ for the crystallographic network and at $p_{cc}^{rand} \approx 0.524$ for the random network. (b) η is fitted to the power-law scaling of Eq. (5) above and below p_{cc}^{crys}.

VII. CONCLUSION

We have simulated grain boundary diffusional creep on a two-dimensional honeycomb grain boundary network, which is composed of low-diffusivity special boundaries and high-diffusivity general boundaries. The dependence of the creep viscosity on the fraction of special boundaries is quantified for both randomly distributed and crystallographically consistent networks. While the percolation thresholds for creep on both types of networks are much lower than the corresponding geometric connectivity thresholds, the percolation threshold for crystallographic networks is somewhat higher than that for random networks. This may provide some guidance for grain boundary engineering procedures that aim to

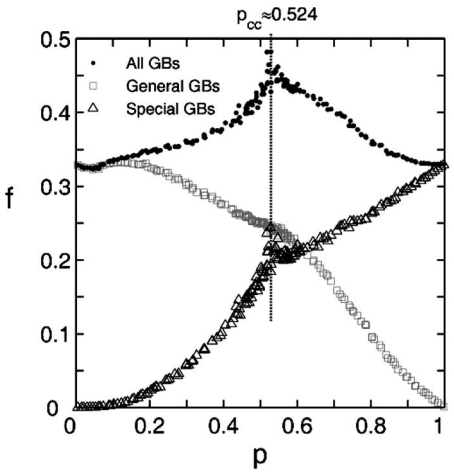

FIG. 11. The fraction f of boundaries with $W-E>0$ [see Eq. (A5) in the Appendix]. The three curves correspond to f for all boundaries as well as for only special boundaries and only general boundaries. The first two cases show a singularity point around the percolation threshold $p_{cc}\approx 0.524$.

control diffusional flow processes at warm to high temperatures.

The percolation scaling properties of Coble creep have been found to conform to the existing notion that crystallographic constraints do not alter the scaling exponents or the percolation universality class. What is unique about Coble creep is that while the exponent below the percolation threshold remains nearly constant over a wide range of special boundary fraction, the exponent above the threshold keeps decreasing with distance from the threshold. The near-threshold scaling exponents are different from the exponents established previously for other percolation problems.

The percolation transition is associated with a shift of the main energy-dissipating species from general to special boundaries. Although the statistical distribution of energy dissipation in general boundaries below the percolation threshold is similar to that in special boundaries above the threshold, the spatial distributions of the energy dissipation on the network in these two cases are distinctly different. The general boundaries that dissipate energy relatively quickly exhibit local morphologies seemingly controlled by diffusion or geometric connectivity; in contrast, the high dissipation rates of the special boundaries originate from the development of a force network that has similar topological characteristics to the rigidity backbone in the elasticity percolation problem. Force balance and transmission by virtue of special boundaries is a critical aspect of the creep problem. The strong correlations among boundary forces revealed by a spatial autocorrelation function also underscore this point.

Special boundaries are special in Coble creep in that they are the force carrying elements on the one hand, and on the other hand, they are the limiting species for both diffusion and plating (matter exchange with grains). It is the coupling between diffusional transport and force balance, or, in other words, the coupling among properties tangential to and normal to the boundary, or, in still other words, the coupling between the lattice and its dual, that seems to be the origin of the complexities and uniqueness of the percolation of Coble creep.

ACKNOWLEDGMENT

This work was supported by the US National Science Foundation under Contract No. DMR-0346848.

APPENDIX: "INTERNAL WORK" VERSUS ENERGY DISSIPATION

The statistical and spatial distributions of the energy dissipation via diffusion along grain boundaries, E, were discussed in Secs. IV B and IV C. Here, the relationship between energy and percolation is examined from a complementary perspective. The total energy dissipation is the summation of E [Eqs. (6)–(8)] over all grain boundaries,

$$\sum E = \sum_{gb} \int_0^1 \delta\Omega \left(J \frac{\partial \sigma}{\partial s} \right) ds = \sum_{gb} \int_0^1 \delta\Omega \frac{\partial (J\sigma)}{\partial s} ds - \sum_{gb} \int_0^1 \delta\Omega \left(\sigma \frac{\partial J}{\partial s} \right) ds. \tag{A1}$$

Applying the divergence theorem[37] to the first term, we find that

$$\sum_{gb} \int_0^1 \delta\Omega \frac{\partial (J\sigma)}{\partial s} ds = \sum_{\text{junction}} \delta\Omega (J_1\sigma_1 + J_2\sigma_2 + J_3\sigma_3). \tag{A2}$$

The integral over grain boundaries reduces to the summation over the junctions in the network; J_1, J_2, and J_3 are the fluxes going from the boundaries into the junction; and σ_1, σ_2, and σ_3 are the stresses acting on the three adjoining boundaries at the junction. At internal triple junctions, $\sigma_1=\sigma_2=\sigma_3$ since the stress has to be continuous, and $J_1+J_2+J_3=0$ because mass must be conserved. At surface junctions, we have imposed a zero flux boundary condition $J_1=J_2=J_3=0$. Thus, Eq. (A2) is equal to zero and Eq. (A1) reduces to

$$\sum E = -\sum_{gb} \int_0^1 \delta\Omega \left(\sigma \frac{\partial J}{\partial s} \right) ds = \sum_{gb} L_{gb} \int_0^1 \sigma V ds = \sum W. \tag{A3}$$

Here, W is defined as the integration of the product of the normal stress σ [Eq. (3)] and the plating rate V [Eq. (2)] over one boundary and is analogous to the concept of internal work in continuum mechanics. Upon the application of the external stress, internal stress is developed in the system and enables the matter plating to occur. As the global summations ΣW and ΣE are both equal to the applied external work, the local value W conceptually represents how much energy one boundary gains and the local value E represents how much energy one boundary dissipates via diffusion per unit time. Thus, $W-E$ is a measure of the local energy balance at one boundary. Introducing Eqs. (2) and (3) into Eq. (A3), we have

$$W = -\frac{\delta\Omega D_{gb}}{KTL_{gb}}\left(\frac{6}{5}{\alpha_3}^2 + 2\alpha_3\alpha_2 + 2\alpha_3\alpha_1 + 3\alpha_3\alpha_0 + \frac{2}{3}{\alpha_2}^2 + \alpha_2\alpha_1 + 2\alpha_2\alpha_0\right) \quad \text{(A4)}$$

and by subtracting Eq. (8), we obtain

$$W - E = -\frac{\delta\Omega D_{gb}}{KTL_{gb}}(3{\alpha_3}^2 + 5\alpha_3\alpha_2 + 4\alpha_3\alpha_1 + 3\alpha_3\alpha_0 + 2{\alpha_2}^2 + 3\alpha_2\alpha_1 + 2\alpha_2\alpha_0 - {\alpha_1}^2). \quad \text{(A5)}$$

In Fig. 11, the fraction of boundaries that "gain" energy (with $W-E>0$) is denoted as f, which is plotted for all boundaries as well as for only general boundaries and only special boundaries. Interestingly, the total fraction of energy-gaining boundaries reaches a maximum of ~0.5 at the percolation threshold p_{cc}. This singular point apparently arises from the divergence of the fraction of special boundaries with $W>E$ at p_{cc} (see triangular points in Fig. 11). Clearly, there is a sudden energy redistribution among the special boundaries at p_{cc}. This is associated with both the increase in W due to the increase of the creep viscosity of the system and the increase and bifurcation in E, as shown in Fig. 8. We suspect that there might be some desired arrangement of the local energy balance in the network that governs the physically percolating event, but more work is needed to clarify the nature of the percolation transition.

*Corresponding author; schuh@mit.edu

[1] D. M. Saylor, B. S. El Dasher, A. D. Rollett, and G. S. Rohrer, Acta Mater. **52**, 3649 (2004).
[2] S. H. Kim, U. Erb, K. T. Aust, and G. Palumbo, Scr. Mater. **44**, 835 (2001).
[3] T. Watanabe and S. Tsurekawa, Acta Mater. **47**, 4171 (1999).
[4] E. M. Lehockey and G. Palumbo, Mater. Sci. Eng., A **237**, 168 (1997).
[5] V. Thaveeprungsriporn and G. S. Was, Metall. Mater. Trans. A **28**, 2101 (1997).
[6] B. Alexandreanu, B. H. Sencer, V. Thaveeprungsriporn, and G. S. Was, Acta Mater. **51**, 3831 (2003).
[7] S. Spigarelli, M. Cabibbo, E. Evangelista, and G. Palumbo, Mater. Sci. Eng., A **352**, 93 (2003).
[8] V. Randle, Acta Mater. **52**, 4067 (2004).
[9] M. Kumar, W. E. King, and A. J. Schwartz, Acta Mater. **48**, 2081 (2000).
[10] T. Watanabe, S. Tsurekawa, X. Zhao, L. Zuo, and C. Esling, J. Mater. Sci. **41**, 7747 (2006).
[11] I. Kaur, W. Gust, and L. Kozma, *Handbook of Grain and Interface Boundary Diffusion Data* (Ziegler, Stuttgart, 1989).
[12] R. Monzen and T. Suzuki, Philos. Mag. Lett. **74**, 9 (1996).
[13] T. Watanabe, M. Yamada, S. Shima, and S. Karashima, Philos. Mag. A **40**, 667 (1979).
[14] I. Kaur and G. Wolfgang, *Fundamentals of Grain and Interphase Boundary Diffusion* (Ziegler, Stuttgart, 1989).
[15] Y. Mishin and C. Herzig, Mater. Sci. Eng., A **260**, 55 (1999).
[16] R. L. Coble, J. Appl. Phys. **34**, 1679 (1963).
[17] W. S. Tong, J. M. Rickman, H. M. Chan, and M. P. Harmer, J. Mater. Res. **17**, 348 (2002).
[18] D. Moldovan, D. Wolf, S. R. Phillpot, A. K. Mukherjee, and H. Gleiter, Philos. Mag. Lett. **83**, 29 (2003).
[19] R. Ding, D. Moldovan, V. Yamakov, D. Wolf, and S. R. Phillpot, Modell. Simul. Mater. Sci. Eng. **13**, 1129 (2005).
[20] Y. Chen and C. A. Schuh, Phys. Rev. Lett. **98**, 035701 (2007).
[21] P. M. Hazzledine and J. H. Schneibel, Acta Metall. Mater. **41**, 1253 (1993).
[22] J. M. Ford, J. Wheeler, and A. B. Movchan, Acta Mater. **50**, 3941 (2002).
[23] M. Frary and C. A. Schuh, Phys. Rev. B **69**, 134115 (2004).
[24] B. N. Kim, K. Hiraga, K. Morita, and I. W. Chen, Philos. Mag. **85**, 2281 (2005).
[25] J. R. Spingarn and W. D. Nix, Acta Metall. **26**, 1389 (1978).
[26] D. Stauffer and A. Aharony, *Introduction to Percolation Theory* (Taylor & Francis, London, 1992).
[27] Y. Chen and C. A. Schuh, Acta Mater. **54**, 4709 (2006).
[28] S. Feng and P. N. Sen, Phys. Rev. Lett. **52**, 216 (1984).
[29] A. R. Day, R. R. Tremblay, and A. M. S. Tremblay, Phys. Rev. Lett. **56**, 2501 (1986).
[30] C. Moukarzel and P. M. Duxbury, Phys. Rev. E **59**, 2614 (1999).
[31] M. Sahimi, *Heterogeneous Materials I: Linear Transport and Optical Properties* (Springer, New York, 2003).
[32] J. J. Wu and D. S. McLachlan, Phys. Rev. B **56**, 1236 (1997).
[33] D. S. McLachlan, W. D. Heiss, C. Chiteme, and J. Wu, Phys. Rev. B **58**, 13558 (1998).
[34] B. W. Reed and M. Kumar, Scr. Mater. **54**, 1029 (2006).
[35] Clinton DeW. Van Siclen, Phys. Rev. B **73**, 184118 (2006).
[36] M. Frary and C. A. Schuh, Acta Mater. **53**, 4323 (2005).
[37] A. Needleman and J. R. Rice, Acta Metall. **28**, 1315 (1980).